PHYSICAL REVIEW FLUIDS **4**, 073501 (2019)

Rotating convection with centrifugal buoyancy: Numerical predictions for laboratory experiments

Susanne Horn[*] and Jonathan M. Aurnou
Department of Earth, Planetary, and Space Sciences, University of California, Los Angeles, California 90095, USA

(Received 11 November 2018; published 19 July 2019)

In Coriolis-centrifugal convection (C^3), buoyancy effects not only drive convective motions in the vertical direction due to the gravitational acceleration but also in the radial direction due to the centrifugal acceleration [Horn and Aurnou, Phys. Rev. Lett. **120**, 204502 (2018)]. Here, we use the flexibility of numerical simulations to vary the gravitational Rossby number $\mathrm{Ro}_{\|}$ and the rotational Froude number Fr independently and thereby study C^3 over the broadest available parameter space. Based on our simulation results we give predictions for laboratory experiments of rotating convection, which inevitably include centrifugal effects. We especially focus on the spatial distribution of the temperature field. Unlike idealized Coriolis convection in which centrifugal buoyancy is neglected, the vertical temperature profiles become strongly radially dependent and exhibit a top-bottom asymmetry with increasing Froude number. In the quasicyclostrophic regime the temperature in the center of the fluid volume shows a strong enhancement, reaching values close to the bottom boundary temperature, whereas the temperatures at the sidewall are well below the arithmetic mean. We find further that the axisymmetric, linear model of Hart and Ohlsen [Phys. Fluids **11**, 2101 (1999)] cannot be used to accurately predict the measured center temperatures, and provide an alternative empirical function based on our fully three-dimensional simulation results. Suggestions are given for the optimal local thermal measurement positions in laboratory experiments to estimate the global heat transfer and the vertical mean-temperature profiles in centrifugally affected rotating convection cases.

DOI: 10.1103/PhysRevFluids.4.073501

I. INTRODUCTION AND THEORETICAL BACKGROUND

Rotating Rayleigh–Bénard convection (RBC) is the canonical system to model the rapidly rotating turbulent convective flows that occur in many geo- and astrophysical environments [1–8]. Rotating RBC consists of a liquid or gasesous layer that is heated from below, cooled from above and rotated around its vertical axis. In the majority of theoretical studies, the Oberbeck-Boussinesq approximation is employed and centrifugal buoyancy effects are ignored [9], which implies a reflection symmetry across the horizontal midplane.

Laboratory and numerical studies are indispensable to gain further insight into rotating RBC in the strongly nonlinear and turbulent state. In experiments, however, the symmetry of the system is often broken leading to far more complex flows. On the one hand, non-Oberbeck-Boussinesq (NOB) effects can break symmetry due to the temperature and pressure dependence of the material properties. NOB effects especially come into play when large temperature gradients are imposed to achieve a strong thermal forcing necessary for turbulence [10–15]. On the other hand, centrifugal buoyancy forces can also break the symmetry of the convective flow [16–25], especially for rapid rotation rates.

---

[*] susannehorn@ucla.edu

2469-990X/2019/4(7)/073501(20) ©2019 American Physical Society

Direct numerical simulations (DNS) have the advantage that they can either solve the idealized Oberbeck-Boussinesq equations without centrifugation, or they may consider more realistic flows with NOB effects [11–14] and centrifugal buoyancy [16,21–25]. Importantly, they allow one to study different physical effects in isolation, including the decoupled investigation of the Coriolis and the centrifugal buoyancy forces. The drawback of DNS are, however, the resolution requirements, in particular, of the ever thinner Ekman boundary layers that prohibit simulations at geo- and astrophysically relevant parameters [6,26–28]. The attainable parameters are usually a couple orders of magnitude less extreme in DNS than in laboratory experiments.

Hence, it is often the synergy between both the numerical and the experimental approaches that allows researchers to make progress. In this spirit, we have recently used DNS to map out the regimes of Coriolis-centrifugal convection (C^3), i.e., thermal convection with the full inertial term [16]. Here, we give numerically based predictions for laboratory studies of rotating convection in which centrifugal buoyancy effects are unavoidably present. These predictions are invaluable because a full parameter coverage of the C^3 system with experiments is cumbersome, if not impossible.

We consider a fluid-filled cylinder with a warm bottom and a cold top boundary that is rotated about its vertical axis with angular velocity $\boldsymbol{\Omega} = \Omega\hat{\mathbf{e}}_z$. We employ the Oberbeck-Boussinesq approximation, where the viscosity ν and the thermal diffusivity κ are held constant. The density ρ cannot be constant, since it is the density difference that drives motion (see Refs. [12,29] for an exact derivation). Instead, ρ is expressed as a Taylor expansion around the mean temperature $T = T_m$, i.e.,

$$\rho = \rho_m(1 - \alpha(T - T_m)), \quad \alpha \equiv -\frac{1}{\rho_m}\frac{\partial \rho}{\partial T}, \tag{1}$$

where α is the isobaric expansion coefficient. In the terms of the Navier-Stokes equation where ρ is a multiplier, ρ can safely be approximated by ρ_m and the higher-order term $\rho_m\alpha(T - T_m)$ can be neglected. In gradient terms, however, the higher-order term of ρ needs to be retained. These gradient terms are the gravitational and the centrifugal acceleration, $-\rho g\hat{\mathbf{e}}_z + \rho\Omega^2 r\hat{\mathbf{e}}_r = \nabla(-\rho g z + \frac{1}{2}\rho\Omega^2 r^2)$; g is the acceleration due to gravity and a cylindrical coordinate system (r, ϕ, z) is considered. The mean parts with ρ_m can be absorbed into the pressure p, while the higher-order terms become the gravitational and centrifugal buoyancy term [24].

The governing equations of C^3 for the velocity $\mathbf{u}$ and the temperature T are the continuity equation, the Navier-Stokes equations with the full inertial term, and the temperature equation. They read

$$\nabla \cdot \mathbf{u} = 0, \tag{2a}$$

$$D_t\mathbf{u} = \nu\nabla^2\mathbf{u} - \nabla p + 2\Omega\mathbf{u} \times \hat{\mathbf{e}}_z - \Omega^2 r\alpha(T - T_m)\hat{\mathbf{e}}_r + g\alpha(T - T_m)\hat{\mathbf{e}}_z, \tag{2b}$$

$$D_t T = \kappa\nabla^2 T. \tag{2c}$$

The last three terms in Eq. (2b) describe the effects of rotation and buoyancy, i.e., the Coriolis, the centrifugal buoyancy and the gravitational buoyancy acceleration. The $\Omega^2 r$ term plays a similar role as the gravitational acceleration g in driving convective motion. Together, they drive cold (denser) fluid downwards and radially away from the axis, whereas warm (less dense) fluid is driven upwards and radially towards the center. The main difference though is that the centrifugal acceleration is not constant in space, causing an intrinsic asymmetry of the system.

In nondimensional form the governing equations become

$$\nabla \cdot \mathbf{u} = 0, \tag{3a}$$

$$D_t\mathbf{u} = \frac{\mathrm{Pr}^{1/2}}{\mathrm{Ra}^{1/2}\gamma^{3/2}}\nabla^2\mathbf{u} - \nabla p + \frac{\gamma^{1/2}}{\mathrm{Ro}_\parallel}\mathbf{u} \times \hat{\mathbf{e}}_z - \mathrm{Fr}\, r\, T\hat{\mathbf{e}}_r + T\hat{\mathbf{e}}_z, \tag{3b}$$

$$D_t T = \frac{1}{\mathrm{Ra}^{1/2}\mathrm{Pr}^{1/2}\gamma^{3/2}}\nabla^2 T, \tag{3c}$$

where we have chosen the radius R, the temperature difference Δ and the velocity $\sqrt{\alpha g \Delta R}$ as the reference scales. The velocity boundary conditions are no-slip on all walls, the sidewall is insulated, and the top and bottom boundaries are isothermal with $T_{\mathrm{top}} = -1/2$ and $T_{\mathrm{bot}} = 1/2$.

The control parameters of RBC are the Rayleigh number, measuring the strength of the gravitational buoyancy force, and the Prandtl number, determining the fluid,

$$\mathrm{Ra} \equiv \frac{\alpha g \Delta H^3}{\kappa \nu}, \quad \mathrm{Pr} \equiv \frac{\nu}{\kappa}. \tag{4}$$

Here Δ is the imposed vertical temperature difference and H is the fluid layer height. Rotation is characterized by the gravitational Rossby number, or alternatively, the Ekman number,

$$\mathrm{Ro}_{\|} \equiv \frac{\sqrt{\alpha g \Delta H}}{2\Omega H}, \quad \mathrm{Ek} \equiv \frac{\nu}{2\Omega H^2} = \sqrt{\frac{\mathrm{Ro}_{\|}^2 \mathrm{Pr}}{\mathrm{Ra}}}. \tag{5}$$

The additional control parameter in the full C^3 system that describes the importance of centrifugation is the rotational Froude number,

$$\mathrm{Fr} \equiv \frac{\Omega^2 R}{g}. \tag{6}$$

The rotational Froude number Fr and the gravitational Rossby number $\mathrm{Ro}_{\|}$ are closely connected through the centrifugal Rossby number,

$$\mathrm{Ro}_{\perp} \equiv \frac{\sqrt{\alpha \Delta}}{2} = \sqrt{\frac{\mathrm{Ro}_{\|}^2 \mathrm{Fr}}{\gamma}} = \sqrt{\frac{\mathrm{Ek}^2\, \mathrm{Ra}\, \mathrm{Fr}}{\mathrm{Pr}\, \gamma}} \quad \text{with } \gamma \equiv \frac{R}{H}, \tag{7}$$

where R is the radius and γ is the radius-to-height aspect ratio.

We solve Eqs. (3) numerically with the fourth-order accurate finite volume code GOLDFISH [16,30] using fixed values of $\mathrm{Pr} = 6.52$, corresponding to water at $T_m = 22.6\,^{\circ}\mathrm{C}$ and $\gamma = 0.365$. We have run two suites of DNS for $\mathrm{Ra} = 10^7$ and 10^8, where we investigated the relative strengths of the Coriolis and centrifugal force for a wide parameter space by varying $0.025 \leqslant \mathrm{Ro}_{\|} \leqslant \infty$ and $0 \leqslant \mathrm{Fr} \leqslant 10$.

We note that Weiss *et al.* [31] and Weiss and Ahlers [32] have shown that 3D convection it weakly influenced by Coriolis forces below a critical Rossby number $\widetilde{\mathrm{Ro}}_{\|}^{W}$. Their analysis semi-empirically determined this bifurcation to occur at

$$\widetilde{\mathrm{Ro}}_{\|}^{W} \simeq \frac{2\gamma}{c_1}\left(1 + \frac{c_2}{2\gamma}\right)^{-1}, \quad c_1 = 0.381,\ c_2 = 0.061. \tag{8}$$

For the DNS presented here, $\widetilde{\mathrm{Ro}}_{\|}^{W} = 1.77$. Accordingly, all flow fields are affected by the Coriolis force to some degree, except for the $\mathrm{Ro}_{\|} = \infty$ cases.

A. Regimes of Coriolis-centrifugal convection

There are four main regimes in the C^3 system [16] that are connected to the three crucial timescales at which the essential dynamics can occur in C^3: the Coriolis timescale τ_{Ω}, the gravitational buoyancy (or free-fall) timescale τ_{ff}, and the centrifugal buoyancy timescale τ_{cb}. These timescales are defined as

$$\tau_{\Omega} = \frac{1}{2\Omega}, \quad \tau_{\mathrm{ff}} = \frac{H}{\sqrt{\alpha \Delta g H}}, \quad \text{and} \quad \tau_{\mathrm{cb}} = \frac{R}{\sqrt{\alpha \Delta \Omega^2 R^2}}, \tag{9}$$

respectively. Figure 1 shows schematically the four main regimes that we have identified based on these timescales [16]:

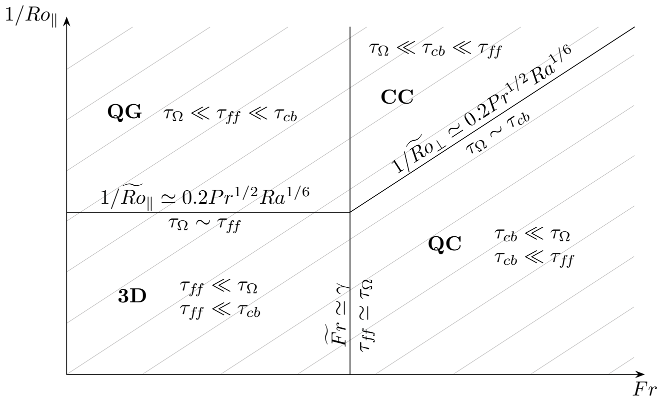

FIG. 1. Regime diagram of Coriolis-centrifugal convection in the inverse gravitational Rossby number $1/\mathrm{Ro}_\parallel$ versus Froude number Fr space: the three-dimensional (3D), quasigeostrophic (QG), quasicyclostrophic (QC), and the Coriolis-centrifugal (CC) regime. The characteristic timescales are defined by Eqs. (9) and the transitions by Eqs. (11) and (12). Laboratory experiments that conduct fixed Ek suites with varying Ra, or fixed Ra suites with varying $\mathrm{Ro}_\parallel$ (and assuming constant material properties) lie along the gray isolines of fixed $\mathrm{Ro}_\perp$.

3D: The flow is fully three-dimensional, i.e., the shortest timescale at which the dominant dynamics occur is τ_{ff}. Thus, it holds that $\tau_{\mathrm{ff}} \ll \tau_\Omega$ and $\tau_{\mathrm{ff}} \ll \tau_{\mathrm{cb}}$. The characteristic flow structures are the large-scale ciculation and mushroom-like plumes [33], shown in Fig. 2(a).

QG: The flow is in quasigeostrophic balance, i.e., the zeroth-order force balance is between the Coriolis and the pressure gradient forces. In first-order balance the gravitational buoyancy is also important. The relevant timescales are ordered as $\tau_\Omega \ll \tau_{\mathrm{ff}} \ll \tau_{\mathrm{cb}}$. For moderate Pr and Ra the typical flow pattern consists of a regular grid of columnar convective Taylor columns [34–36], shown in Fig. 2(b).

QC: The flow is in quasicyclostrophic balance, i.e., the primary force balance is between the centrifugal buoyancy and the pressure gradient forces. The order of the governing timescales is $\tau_{\mathrm{cb}} \ll \tau_\Omega$ and $\tau_{\mathrm{cb}} \ll \tau_{\mathrm{ff}}$. The archetypal flow is an axisymmetric meridional circulation [17,24], shown in Fig. 2(c).

(a) LSC and plumes

(b) Convective Taylor columns

(c) Meridional circulation

FIG. 2. Prototypal flow components in Coriolis-centrifugal convection. Shown are temperature isosurfaces for $\mathrm{Ra} = 10^8$. The respective flow configuration is sketched with black lines and arrows demarcating (a) the large-scale circulation with mushroomlike plumes ($\mathrm{Ro}_\parallel = \infty$, $\mathrm{Fr} = 0$); (b) the space-filling convective Taylor columns ($\mathrm{Ro}_\parallel = 0.05$, $\mathrm{Fr} = 0$); (c) the donut-shaped, axisymmetric meridional circulation ($\mathrm{Ro}_\parallel = \infty$, $\mathrm{Fr} = 0.5$). (See Fig. 5 for their respective 2D slices.)

CC: The flow is geostrophic to zeroth order. In first-order balance, the centrifugal buoyancy forces requires consideration. The ordering of the dynamically important timescales is $\tau_\Omega \ll \tau_{\mathrm{cb}} \ll \tau_{\mathrm{ff}}$. These flows show characteristics of both the QG and QC regime, as well as ring structures [16].

The timescales (9) also define the transition parameters between these regimes. The transition from the 3D regime to the QG regime is well-studied and may be expressed in terms of a critical gravitational Rossby number $\widetilde{\mathrm{Ro}}_\parallel = \tau_\Omega/\tau_{\mathrm{ff}}$. Here, we use the criterion by King *et al.* [37] that defines the border between 3D and QG flows through the cross-over of the thermal and viscous boundary layers, yielding

$$6 \lesssim \mathrm{Pr}^{3/4}\mathrm{Ra}^{1/4}\widetilde{\mathrm{Ro}}_\parallel^{3/2} \lesssim 20. \tag{10}$$

Alternative methods based on different output quantities, such as the Nusselt number or the toroidal and poloidal energies, yield commensurable results for the transition range [2,8,11,31,38] and these methods are also valid for $\mathrm{Pr} < 1$ fluids. As the transition parameter between the QC and CC regime, we put forward that the critical centrifugal Rossby number $\widetilde{\mathrm{Ro}}_\perp = \tau_\Omega/\tau_{\mathrm{cb}}$ is equal to $\widetilde{\mathrm{Ro}}_\parallel$. In the following we will use the respective mean values of the approximate transition ranges,

$$\widetilde{\mathrm{Ro}}_\parallel \simeq 5.5\,\mathrm{Pr}^{-1/2}\mathrm{Ra}^{-1/6}, \quad \widetilde{\mathrm{Ro}}_\perp \simeq 5.5\,\mathrm{Pr}^{-1/2}\mathrm{Ra}^{-1/6}, \tag{11}$$

for the sake of simplicity and clarity.

We argue that the intersection of both Rossby numbers, $\widetilde{\mathrm{Ro}}_\parallel \simeq \widetilde{\mathrm{Ro}}_\perp$, specifies the critical Froude number $\widetilde{\mathrm{Fr}}$ for the transition to centrifugally dominated dynamics [16]. This implies

$$\widetilde{\mathrm{Fr}} \simeq \gamma, \tag{12}$$

which dimensionally is equivalent to a critical height $\widetilde{H} \simeq g/\Omega^2$ above which centrifugation should dominate. Thus, we posit that in slender and tall convection vessels deceptively small centrifugal forces can significantly alter the results. These predictions were corroborated by global Nusselt number analyses [16]. Furthermore, one can define the superfroudeality as

$$\chi \equiv \frac{\mathrm{Fr}}{\widetilde{\mathrm{Fr}}} = \frac{\mathrm{Fr}}{\gamma} = \frac{\tau_{\mathrm{ff}}^2}{\tau_{\mathrm{cb}}^2}, \tag{13}$$

where $\chi \gtrsim 1$ denotes the domination of centrifugal over gravitational buoyancy.

II. THE TEMPERATURE DISTRIBUTION IN CORIOLIS-CENTRIFUGAL CONVECTION

Here we investigate the spatial distribution of the temperature field in C^3, following Horn and Aurnou [16]. Our results are particularly relevant for the present state-of-the-art multi-meter convection devices that seek to characterize the QG-turbulence regime [4].

Temperature profiles are one of the most common output quantities that both numerical and laboratory studies evaluate [e.g., [30,39–49]], because they can be used to draw important conclusions about the interior and boundary dynamics of the system [e.g., [26,46,50–53]]. Examples include distinguishing between a well-mixed turbulent bulk and a more vertically than laterally mixed bulk in rotating convection [39,54]; the search for logarithmic profiles as precursors of the ultimate state of turbulent Rayleigh-Bénard convection [55–57]; quantifying thermal boundary layer properties [58]; and measurements of the Nusselt number [42].

In numerical simulations, where the full 3D temperature information is available, mean-temperature profiles are usually obtained by horizontal plane and time averages, $\bar{T}(z) = \langle T(r,\phi,z,t)\rangle_{r,\phi,t}$. In most laboratory studies, only pointwise thermal field measurements are available due to the natural limitation in the number of thermistors/thermocouples, and necessarily these profiles require approximation. However, due to the turbulent and spatiotemporally varying nature of the flow, these approximations are usually accurate for long laboratory data acquisitions.

Local thermal measurements, especially of the center temperature T_c, provide a straightforward way of validating an experimental setup. T_c is an excellent measure for quantifying asymmetries of the system, such as NOB effects [10–14]. In NOB convection of liquids, T_c is generally higher than the arithmetic mean T_m. In the NOB case, evaluating the material properties at T_c instead of T_m allows one to still obtain reliable results that are in good ingreement to OB measurements [12,59].

Centrifugal buoyancy is known to alter the temperature field due to the generation of a meridional circulation, as visualized in Fig. 2(c). It is, however, unknown whether local measurements can still adequately approximate the global mean properties of the flow. The only theoretical attempt to quantify the implications of the centrifugally driven meridional circulation on the mean-temperature profiles and the center temperature was made by Hart and Ohlsen [17] [cf. [18]]. Their main finding is that the meridional circulation leads to a positive thermal offset $T_c - T_m$. The Hart and Ohlsen model is summarized in Sec. II D. While this model is often employed to predict the center temperature, it has, in fact, not yet been systematically tested. We aim to rectify this omission. Further, our goal is to provide a roadmap for current and future laboratory experiments of turbulent thermal rotating convection. We give predictions in which way (enhancement/diminishment) thermal properties change; how they depend on the measurement positions; whether there are ideal locations for the placement of thermistors and thermocouples in the flow.

A. Accessible parameter space of Coriolis-centrifugal convection by laboratory experiments

The parameter space of C^3 in the $\mathrm{Ro}_{\parallel}$-Fr plane that is accessible in a given laboratory experiment is greatly restricted relative to DNS. Hence, we first evaluate which regimes of C^3 are within reach for a specific setup.

It is assumed that the working fluid is water at $T_m = 22.6\,^{\circ}\mathrm{C}$ with $\mathrm{Pr} = 6.52$ and that the convection tank has an aspect ratio of $\gamma = 0.365$, as used in the present DNS. The material properties of water at this mean temperature are $\alpha = 2.334 \times 10^{-4}\ \mathrm{K}^{-1}$, $\nu = 9.499 \times 10^{-7}\ \mathrm{m}^2/\mathrm{s}$, and $\kappa = 1.457 \times 10^{-7}\ \mathrm{m}^2/\mathrm{s}$; the gravitational acceleration is $g = 9.81\ \mathrm{m}/\mathrm{s}^2$ [10,11].

Further, in accordance with our DNS, we will assume that surveys of constant Ra are desired and that the height H of the convection cell is fixed. To obtain moderate $\mathrm{Ra} = 10^8$ in the laboratory, the tank needs to be relatively short. We will consider three virtual convection cells of height $H_1 = 5$ cm, $H_2 = 10$ cm, and $H_3 = 20$ cm, as sketched in Fig. 3. The constraint through Ra and H, thus, determines the temperature difference that needs to be imposed by

$$\Delta = \frac{\kappa \nu}{\alpha g H^3} \mathrm{Ra}, \tag{14}$$

and gives $\Delta_1 = 48.3$ K, $\Delta_2 = 6.0$ K, and $\Delta_3 = 0.8$ K. Fixing the same gravitational Rossby numbers as in the DNS, $\mathrm{Ro}_{\parallel} \in \{0.025,\ 0.05,\ 0.1,\ 0.5,\ 1.0\}$, is then achieved by setting the rotation rate according to

$$\Omega = \frac{\sqrt{\alpha g \Delta H}}{2H} \mathrm{Ro}_{\parallel}^{-1}. \tag{15}$$

The resulting points in the $\mathrm{Ro}_{\parallel} - \mathrm{Fr}$ phase are shown in Fig. 3. The rotation rate Ω and also the temperature difference Δ are limited by the device, by phase transitions of the material and by the aim to preferably keep NOB effects small. If we demand $0.5\ \mathrm{K} \leqslant \Delta \leqslant 45\ \mathrm{K}$ and $1\ \mathrm{rpm} \leqslant \Omega \leqslant 100\ \mathrm{rpm}$, then only the virtual cell of height $H_2 = 10$ cm can reach all five different $\mathrm{Ro}_{\parallel}$. The relation between Fr and $\mathrm{Ro}_{\parallel}$ through $\mathrm{Ro}_{\perp}$, Eq. (7), however, only allows scanning the full C^3 parameter space along isolines of $\mathrm{Ro}_{\perp}$. Thus, exploring the phase space in Fr for a constant $\mathrm{Ro}_{\parallel}$ requires another tank with a different dimensional height H, but the same aspect ratio γ. Figure 3 further shows that except for the tallest virtual tank with 20 cm the CC and the QC regime can not be reached in the laboratory at that low $\mathrm{Ra} = 10^8$ value.

We can generalize these results, and we present the resulting accessible range in C^3 for the three different Rayleigh numbers $\mathrm{Ra} = 10^9$, 10^{11}, and 10^{13} in Fig. 4. In functional form, the accessible

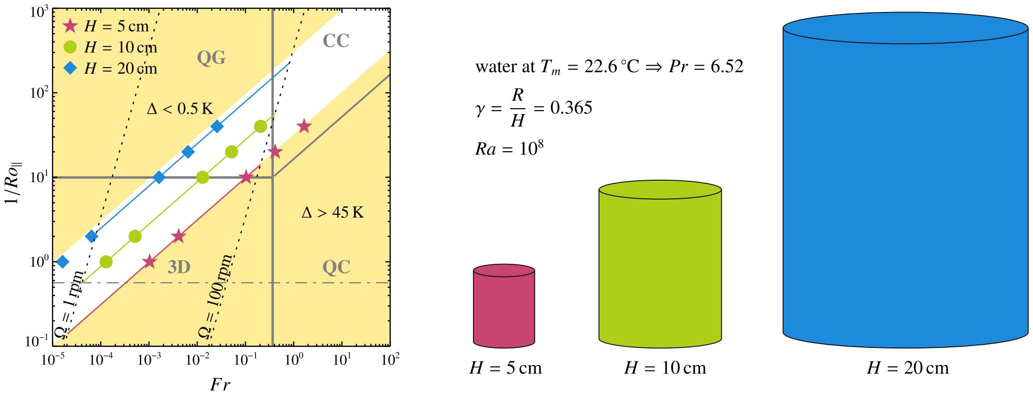

FIG. 3. Regime diagram for water at a mean temperature of $T_m = 22.6\ ^\circ\mathrm{C}$, corresponding to $\mathrm{Pr} = 6.52$, and a fixed aspect ratio of $\gamma = 0.365$ and Rayleigh number of $\mathrm{Ra} = 10^8$, as in our DNS. The regime boundaries according to the Eqs. (11) and (12) are marked by the gray solid lines. The transition to weakly Coriolis affected flows according to Eq. (8) is marked by the gray dash-dotted line. In laboratory experiments the accessible range is given by the maximum employable temperature difference Δ and rotation rate Ω. Here we assume $0.5\ \mathrm{K} \leqslant \Delta \leqslant 45\ \mathrm{K}$ and $1\ \mathrm{rpm} \leqslant \Omega \leqslant 100\ \mathrm{rpm}$. The intimate relation of $\mathrm{Ro}_\parallel$ and Fr through $\mathrm{Ro}_\perp$ [Eq. (7)] and consequently Δ restricts the permissible range to values within the white strip, i.e., within $\mathrm{Ro}_\perp = \sqrt{\alpha\Delta}/2 = 5.4 \times 10^{-3}$ and 5.1×10^{-2}, the upper yellow area indicates $\Delta < 0.5$ K and the lower yellow are $\Delta > 45$ K. Furthermore, Ω restricts the range through the definition of Fr and $\mathrm{Ro}_\parallel$ and assuming $\Delta = \mathrm{Ra}\,\kappa\nu/(\alpha g h^3)$, where h are all possible heights. The pink, green, and blue lines show the theoretical values for three different virtual convection cells of fixed heights 5 cm, 10 cm, and 20 cm and $1\ \mathrm{rpm} \leqslant \Omega \leqslant 100\ \mathrm{rpm}$ within the $\mathrm{Ro}_\parallel$-Fr space. For fixed Ra, only experiments along isolines of $\mathrm{Ro}_\perp$ are possible. For DNS there are no restrictions in the $\mathrm{Ro}_\parallel$-Fr space, including the possibilities ($\mathrm{Ro}_\parallel = \infty$, $\mathrm{Fr} \neq 0$) and ($\mathrm{Ro}_\parallel < \infty$, $\mathrm{Fr} = 0$). The symbols correspond to $\mathrm{Ro}_\parallel \in \{0.025,\ 0.05,\ 0.1,\ 0.5,\ 1.0\}$ that are studied here with DNS mapped to the virtual convection tanks.

parameter space is generally limited by $\Delta^{\mathrm{low}} \leqslant \Delta \leqslant \Delta^{\mathrm{high}}$ through

$$\mathrm{Ro}_\parallel^{\mathrm{low}} = \mathrm{Ro}_\perp^{\mathrm{low}}\sqrt{\frac{\gamma}{\mathrm{Fr}}} = \sqrt{\frac{\alpha\Delta^{\mathrm{low}}\gamma}{4\,\mathrm{Fr}}}, \tag{16}$$

$$\mathrm{Ro}_\parallel^{\mathrm{high}} = \mathrm{Ro}_\perp^{\mathrm{high}}\sqrt{\frac{\gamma}{\mathrm{Fr}}} = \sqrt{\frac{\alpha\Delta^{\mathrm{high}}\gamma}{4\,\mathrm{Fr}}}, \tag{17}$$

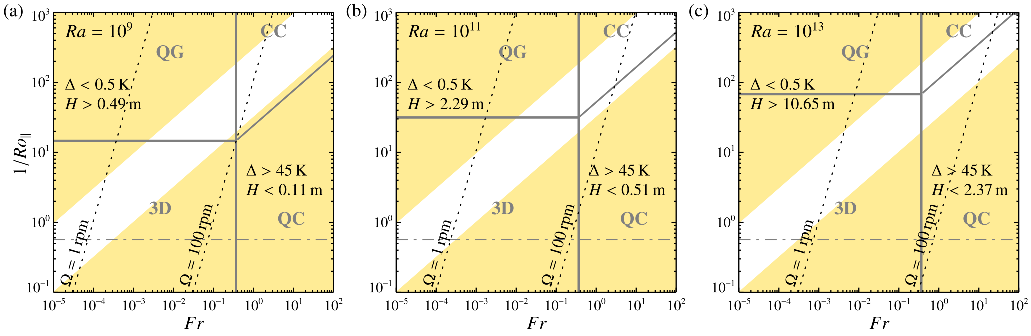

FIG. 4. Similar to Fig. 3, showing the experimentally accessible range for fixed (a) $\mathrm{Ra} = 10^9$, (b) $\mathrm{Ra} = 10^{11}$, and (c) $\mathrm{Ra} = 10^{13}$.

marked by the yellow shaded area in Figs. 3 and 4. This also limits the height H, according to the definition of Ra. The rotation rate Ω restricts this area further, according to the definitions of $\mathrm{Ro}_{\|}$ and Fr. The transition to centrifugally dominated dynamics also shifts with Ra according to Eq. (11). Figure 4 shows that for higher Ra, which are easily achieved by present multi-meter laboratory devices [4], the QC and CC regime can be probed. Hence, understanding the temperature distribution in these regimes is indeed important and relevant.

B. Flow morphologies

Knowing the fundamental flow configurations is crucial for the understanding and interpretation of the temperature distribution, in particular, the vertical profiles of the temperature field, the center temperature and the local heat flux at the boundaries. Figure 5 shows a selection of characteristic flow fields for $\mathrm{Ra} = 10^8$ covering the $\mathrm{Ro}_{\|}$-Fr space. The Coriolis force increases with inverse $\mathrm{Ro}_{\|}$ from bottom to top and the centrifugal force increases with Fr from left to right. For $\mathrm{Ro}_{\|} = \infty$, the Coriolis force vanishes, whilst the centrifugal force vanishes for $\mathrm{Fr} = 0$. In addition, the proposed regime boundaries [16] are marked by gray lines in Fig. 5. According to Eq. (10), the transition between the 3D and QG regime occurs at $0.06 \lesssim \widetilde{\mathrm{Ro}}_{\|} \lesssim 0.13$ for $\mathrm{Ra} = 10^8$. Correspondingly, the transition between the QC and CC regime takes place at $0.06 \lesssim \widetilde{\mathrm{Ro}}_{\perp} \lesssim 0.13$ for $\mathrm{Ra} = 10^8$. [For clarity we only show the average value [Eq. (11)] in all the figures herein.] The border from the 3D and QG regime to the centrifugally dominated regimes QC and CC is demarcated by $\widetilde{\mathrm{Fr}} \simeq \gamma = 0.365$. None of these transitions are expected to be sharp, but should happen over a relatively broad range.

When both rotational forces are small or zero, i.e., $\mathrm{Ro}_{\|} \gtrsim \widetilde{\mathrm{Ro}}_{\|}$ and $\mathrm{Fr} < \gamma$, the flow is three-dimensional (3D), as can be seen in the lower left corner of Fig. 5. The prevalent flow structures are plumes and the LSC [33,60]. With increasing Coriolis force, i.e., decreasing $\mathrm{Ro}_{\|}$, the LSC breaks down, the plumes become more vortical, and eventually they transform into convective Taylor columns [11,34,35,61–63]. The flow fields in the fully Coriolis-dominated QG regime, i.e., $\mathrm{Ro}_{\|} \lesssim \widetilde{\mathrm{Ro}}_{\|}$ and $\mathrm{Fr} < \gamma$, are depicted in the upper left corner of Fig. 5. The 3D and the QG regime have been investigated in great detail by a number of researchers [e.g. [3,5,7,8,11,31,36,39,41, 62–70]] and are therefore not the focus of the present work.

Our attention is chiefly devoted to the centrifugally affected flows. In the lowermost row of Fig. 5 where $\mathrm{Fr} > \gamma$ and $\mathrm{Ro}_{\|} = \infty$, rotation only acts on the flow through the centrifugal buoyancy force and the Coriolis force is identically zero. We observe an almost axisymmetric meridional circulation, characterized by a hot collimated central jet and a lower velocity cold downwelling along the sidewall. Several previous studies [e.g., Ref. [17,21]], thus, assumed an axisymmetric flow. However, even in this idealized $\mathrm{Ro}_{\|} = \infty$ case, small azimuthal instabilities are visible close to the walls. These instabilities become rather pronounced for $\mathrm{Fr} = 2$ (see Ref. [16]). When centrifugal buoyancy is much stronger than gravitational buoyancy, $\mathrm{Fr} = 10$, shown in the bottom right corner of Fig. 5, the horizontal temperature gradient between the hot central upwelling and cold down flow along the sidewall is almost of the same magnitude as the vertical temperature gradient. As a result, the flow exhibits similar convective instabilities as found in vertical convection [71,72].

Moving upwards in Fig. 5, but still in the QC regime, i.e., $\mathrm{Ro}_{\|} < \widetilde{\mathrm{Ro}}_{\|}^{W}$, $\mathrm{Ro}_{\perp} \lesssim \widetilde{\mathrm{Ro}}_{\perp}$ and $\mathrm{Fr} > \gamma$, the secondary influence of the Coriolis force causes a helical modulation of the central jet of the meridional circulation. The flow structures can be described as tornado-like vortices [73–76]. For $\mathrm{Fr} = 10$ and $\mathrm{Ro}_{\|} \lesssim 0.1$, shown in the uppermost right corner, the QC flow has almost fully laminarized as both Coriolis and centrifugal force generally tend to suppress turbulent fluctuations.

Finally, the three cases in the CC regime, i.e., $\mathrm{Ro}_{\|} = 0.05$, $\mathrm{Fr} = 0.5$; $\mathrm{Ro}_{\|} = 0.05$, $\mathrm{Fr} = 1.0$; and $\mathrm{Ro}_{\|} = 0.1$, $\mathrm{Fr} = 0.5$, reveal a superposition of an overturning circulation and ring-like structures with a strong azimuthal velocity component. A few cases for $\mathrm{Ra} = 10^7$ (not shown) also possess a central downdraft. Thus, the characteristic flows qualitatively resemble hurricanes, including a warm eye in the center and multiple eye walls [77].

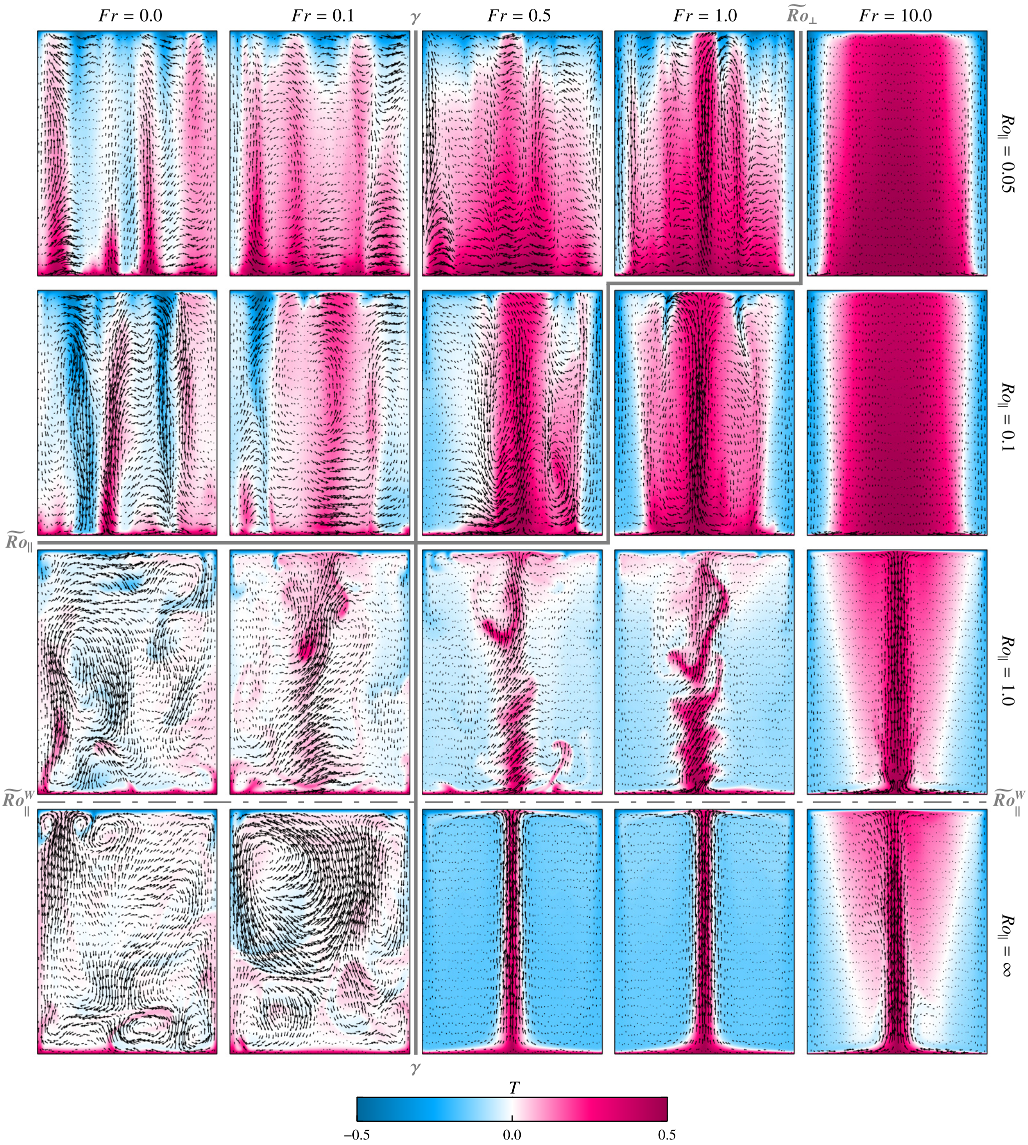

FIG. 5. Instantaneous vertical cross-sections of the temperature field with overplotted velocity vectors for fixed $\mathrm{Ra} = 10^8$, $\mathrm{Pr} = 6.52$, and $\gamma = 0.365$. $\mathrm{Ro}_\parallel \in \{\infty, 1.0, 0.1, 0.05\}$ decreases from bottom to top, characterizing the increasing Coriolis force, $\mathrm{Fr} \in \{0.0, 0.1, 0.5, 1.0, 10.0\}$ increases from left to right, characterizing the increasing centrifugal buoyancy force. $\mathrm{Fr} = 0.0$ corresponds to zero centrifugal force, $\mathrm{Ro} = \infty$ to zero Coriolis force cases. The predicted regime boundaries according to Horn and Aurnou [16] are marked with the gray lines, where the full vertical line corresponds to $\mathrm{Fr} = \gamma$, the full horizontal line to $\widetilde{\mathrm{Ro}}_\parallel = 0.1$ and the zigzag line to $\widetilde{\mathrm{Ro}}_\perp = 0.1$ according to Eqs. (11). The dash-dotted line is the prediction by Weiss *et al.* [31], given by Eq. (8).

C. Temperature profiles

The temperature distribution is quantified by calculating the local vertical temperature profiles $\bar{T}_l(r, z) \equiv \langle T(t, r, \phi, z)\rangle_{t,\phi}$ and the mean-vertical-temperature profile $\bar{T}(z) \equiv \langle T(t, r, \phi, z)\rangle_{t,r,\phi}$. Figure 6 shows the local profiles $\bar{T}_l(r, z)$ obtained for every radial position as well as $\bar{T}(z)$ from our DNS for $\mathrm{Ra} = 10^8$ for the same cases as the flow fields displayed in Fig. 5.

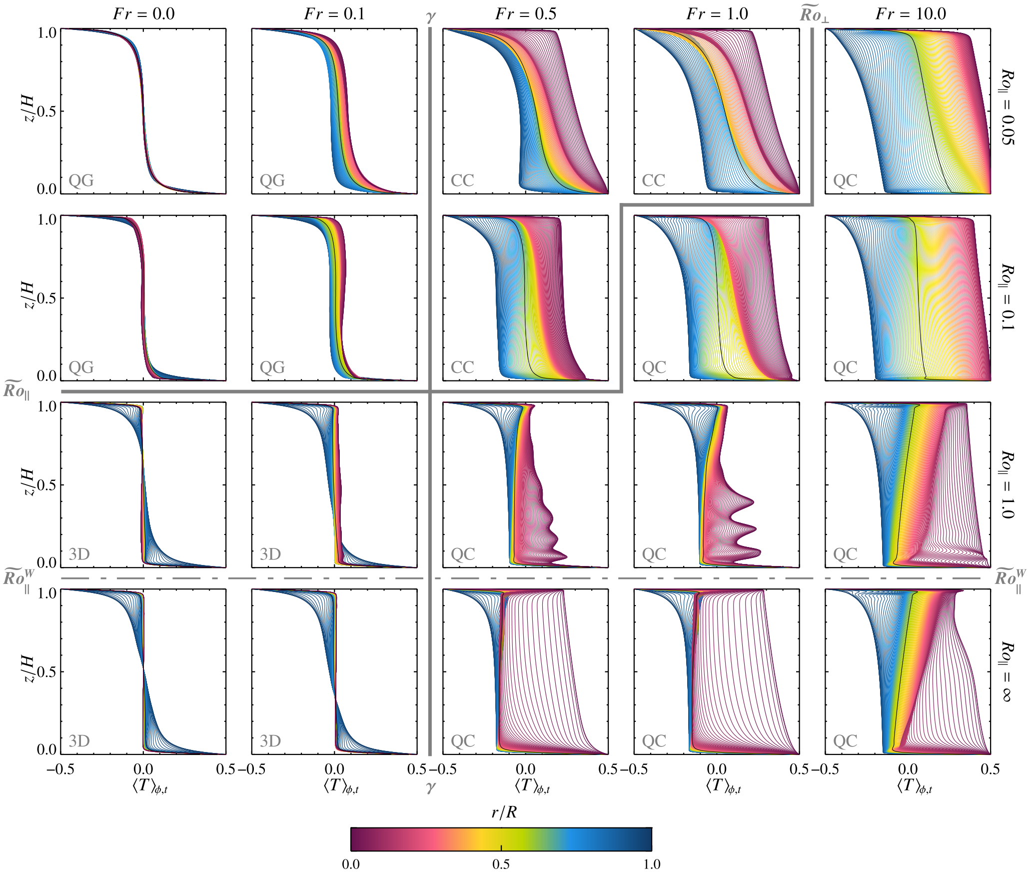

FIG. 6. Azimuthally and temporally averaged temperature profiles $\langle T \rangle_{\phi,t}$. The color indicates the radial position where the profile is obtained, ranging from the center, $r/R = 0.0$, to the sidewall, $r/R = 1.0$. The black solid lines demarcate the plane-averaged temperature profile $\bar{T}(z) = \langle T \rangle_{t,r,\phi}$. $\mathrm{Ro}_\parallel \in \{\infty,\ 1.0,\ 0.1,\ 0.05\}$ decreases from bottom to top, $\mathrm{Fr} \in \{0.0,\ 0.1,\ 0.5,\ 1.0,\ 10.0\}$ increases from left to right. The gray lines correspond to the regime boundaries as in Fig. 5.

In the 3D regime (lower left corner of Fig. 6), the local profiles $\bar{T}_l(r, z)$ in the bulk, $r/R \lesssim 0.9$, and $\bar{T}(z)$ are approximately congruent; only the profiles close to the sidewall $r = R$ deviate and have a shallower slope $\partial_z \bar{T}_l$. This deviation is known to be due to the corner rolls at the sidewall that act to inhibit the heat transport [78]. In the QG regime, shown in the upper left part of Fig. 6, all local profiles approximate the mean-temperature profile and the mean-temperature gradient at midheight very well.

The congruency between the mean- and local-temperature profiles is lost in the centrifugally dominated regimes in the right part of Fig. 6 where $\mathrm{Fr} > \gamma$. The stronger the centrifugal buoyancy effects are, the less representative local measurements along only one radial position become for the mean profile. Thus, in the QC and CC regimes, the local profiles and also the central vertical temperature gradient display a strong radial dependence and a broken top-bottom symmetry.

There are no universal trends discernible in the $\mathrm{Fr} > \gamma$ temperature profiles. When the Coriolis force is absent, i.e., $\mathrm{Ro}_\parallel = \infty$, as shown in the lowermost row of Fig. 6, only the temperature profiles obtained close to the axis at $r = 0$ contain positive temperatures in the fluid bulk. The majority of these profiles, including the mean-temperature profile, have negative temperatures throughout the bulk. Except for the negative offset, the $\mathrm{Ro}_\parallel = \infty$ profiles for $\mathrm{Fr} = 0.5$ and $\mathrm{Fr} = 1.0$ exhibit a

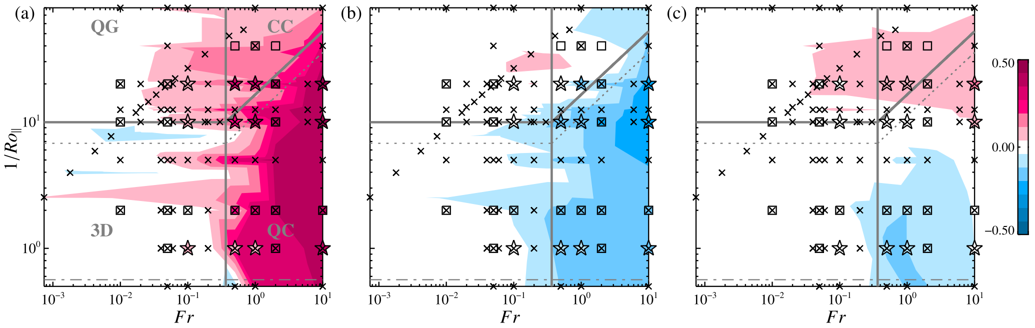

FIG. 7. Center temperature T_c obtained by DNS; (a) evaluated at the axis, $T_c^a \equiv \langle T(r=0, z=H/2)\rangle_t$; (b) based on a sidewall average, $T_c^{\mathrm{sw}} \equiv \langle T(r=R, z=H/2)\rangle_{t,\phi}$; (c) defined as a midplane average, $T_c^{\mathrm{pl}} \equiv \langle T(z=H/2)\rangle_{r,\phi,t}$. The gray lines correspond to the regime boundaries as in Fig. 5, the dotted lines correspond to $\widetilde{\mathrm{Ro}}_\parallel$ and $\widetilde{\mathrm{Ro}}_\perp$ for $\mathrm{Ra} = 10^7$, the solid lines to $\mathrm{Ra} = 10^8$. The phase diagrams are based on the $\mathrm{Ra} = 10^7$ data due to the larger coverage in the Fr-$\mathrm{Ro}_\parallel$ space. The filled symbols correspond to the $\mathrm{Ra} = 10^8$ data set, with the stars marking the selected cases shown in Figs. 5, 6, and 9.

close similarity to the $\mathrm{Fr} = 0$ case for $r/R \gtrsim 0.2$, especially in the upper half of the cylinder. The mean-temperature gradient $\partial_z T_m$ in all $\mathrm{Ro}_\parallel = \infty$ cases is positive, and enhances with Fr.

Most of the $\mathrm{Ro}_\parallel = \infty$ behaviors carry over to the weakly Coriolis affected cases in the QC regime for $\mathrm{Ro}_\parallel = 1.0$ and $\mathrm{Fr} > \gamma$. At the outer radii, the local profiles in the tornado-like cases are morphologically similar to the $\mathrm{Fr} < \gamma$ and $\mathrm{Ro}_\parallel = \infty$ cases. Only in the lower central part of the cylinder are the profiles modulated by the helical upwelling. Time averaging was done for several hundred free-fall time units and, thus, it seems unlikely that the helical modulations will ever completely average out.

For the $\mathrm{Fr} = 10$, $\mathrm{Ro}_\parallel = \infty$, and $\mathrm{Ro}_\parallel = 1$ cases, shown in the lower right side of Fig. 6, the strong radial centrifugation and the induced radial shear along the boundaries produce an overshoot in $\bar{T}(z)$ close to the top and bottom of the fluid layer.

The appearance for the profiles qualitatively changes for $\mathrm{Ro}_\parallel < \widetilde{\mathrm{Ro}}_\parallel$, shown in the panels in the upper half of Fig. 6. The mean-temperature profiles are generally positive in the bulk and the vertical mean-temperature gradient reverses its sign along this line. With increasing Fr, the radial distribution of the temperature profiles becomes broader, without any clear preference of a radial position.

For laboratory experiments, this implies that local measurements along only one constant radius, such as sidewall or center measurements, become less representative of the mean profile in $\mathrm{Fr} \gtrsim \gamma$ flows. It is also clear that the vertical temperature profiles have a strong top and bottom asymmetry. Thus, it does not suffice to only measure in one half of the cylinder and assume a mirror antisymmetry. It also means that any theoretical model will need to take this asymmetry into account.

Interestingly, the transition border given by $\widetilde{\mathrm{Ro}}_\perp$ appears to be insignificant for the mean-temperature profiles. However, it remains crucial for specific radial positions, including at the sidewall and the center, as we will elucidate next using pointwise representations of the temperature calculated at midheight.

D. The center temperature

Figure 7 presents three common measures for the center temperature. All of them are known to yield the exact arithmetic mean between top and bottom temperature when centrifugal buoyancy is not present, $\bar{T} = (T_{\mathrm{top}} + T_{\mathrm{bot}})/2 = 0$. A deviation from $\bar{T} = 0$ is called a "thermal offset" [17]. The evaluated midheight temperatures are the temperature at the axis $T_c^a \equiv \langle T(r=0, z=H/2)\rangle_t$, the sidewall temperature $T_c^{\mathrm{sw}} \equiv \langle T(r = R, z = H/2)\rangle_{t,\phi}$, and the plane averaged temperature $T_c^{\mathrm{pl}} \equiv \langle T(z = H/2)\rangle_{r,\phi,t}$.

The first two definitions, T_c^a and T_c^{sw}, trace the previously defined regimes satisfactorily [16], but with completely opposite trends. Thus, T_c^a shows a positive thermal offset, while T_c^{sw} shows a negative thermal offset. The plane average, on the other hand, shows a separation along $\mathrm{Ro}_\parallel \sim \widetilde{\mathrm{Ro}}_\parallel$. For $\mathrm{Ro}_\parallel \gtrsim \widetilde{\mathrm{Ro}}_\parallel$, we have $T_c^{\mathrm{pl}} < 0$ and for $\mathrm{Ro}_\parallel \lesssim \widetilde{\mathrm{Ro}}_\parallel$, we have $T_c^{\mathrm{pl}} > 0$.

Hart and Ohlsen [17] developed an axisymmetric model to describe the thermal offset in the case of rapid rotation and nonnegligible centrifugal buoyancy. The model assumes that the center temperature is constant along the entire midplane, which implies that all three definitions of T_c shown in Fig. 7 should amount to the same value. In testing their model against our DNS results, we have chosen our T_c^a values, which has their expected sign of T_c and, thus, should compare most favorably of the three possible central temperature definitions. We recapitulate the essentials of the Hart and Ohlsen [17] model in the following.

The main assumption of the model is that the vertical mean-temperature profile T_m can be approximated as

$$T_m(z) = -bz - (1-b)\frac{\sinh(\zeta z)}{2\sinh\left(\frac{\zeta}{2}\right)}, \qquad \text{with } \zeta \equiv \frac{2(\mathrm{Nu}-b)}{1-b}, \tag{18}$$

and where b is the mean-core-temperature gradient and $-1/2 \leqslant z \leqslant 1/2$, assuming H as reference length. The first summand describes the bulk contribution and the second one the boundary layer contribution. The temperature gradient b as well the Nusselt number Nu are input parameters obtained from DNS or laboratory experiments. The full axisymmetric temperature field is given by $T = T_m + \mathrm{Pr}\,\theta(r, z, t)$, where θ is the temperature perturbation. The boundary conditions are $T|_{z=\pm 1/2} = T_m|_{z=\pm 1/2} = \mp 1/2$ and $\theta|_{z=\pm 1/2} = 0$.

Following Hart and Ohlsen [17] [cf. Refs. [79,80]], the linearized set of equations that describes the centrifugal circulation (indicated by the subscript cc) can be obtained by means of the similarity reduction of the axisymmetric flow variables, $u_r = r\,U_{cc}(z)$, $u_\phi = r\,V_{cc}(z)$, $u_z = W_{cc}(z)$, $\theta = \Theta_{cc}(z)$. In this model, the radial and vertical velocity are scaled with ν/H, the azimuthal velocity with $2\Omega H$ and the temperature with Δ. The resulting set of ordinary differential equations is given by

$$U_{cc}'' + 4\eta^4 V_c = 4\mathrm{Ro}_\perp^2\,\eta^4\,T_m, \quad U_{cc} = V_{cc}'', \quad W_{cc}' = -2U_{cc}, \quad \Theta_{cc}'' = W_{cc}\,T_m', \tag{19}$$

with $\eta \equiv (2\mathrm{Ek})^{-1/2}$; the primes denote ordinary derivatives with respect to z. Equations (19) can be solved analytically. Since the full solution was not given explicitly by Hart and Ohlsen [17], we provide it in the Supplemental Material, including a `fortran` routine [81] that solves for the center temperature $\Theta_{cc}(0) = T_c/\mathrm{Pr}$ for any given η, ζ, and b.

Hart and Ohlsen [17] also give a simplified version that is valid in the limit $\zeta^2 \gg \mathrm{Ek}^{-1}$, which holds for large Nu. The contribution from the boundary layers is neglected in this limit and the centrifugal circulation is only determined by the temperature gradient b. This leads to a simpler set of equations, including a more tractable relation for $\Theta_{cc}(0)$. An equivalent formulation of the original equation by Hart and Ohlsen [17] (cf. Ref. [18]) for the center temperature T_c^{HO} is

$$\begin{aligned} T_c^{\mathrm{HO}} &= \mathrm{Pr}\,\Theta_{cc}(0) \\ &= \mathrm{Pr}\,b^2\mathrm{Ro}_\perp^2\,\frac{(\eta^2+4)\sin(\eta) + (\eta^2-4)\sinh(\eta) + 8\cos\left(\frac{\eta}{2}\right)\sinh\left(\frac{\eta}{2}\right) - 8\sin\left(\frac{\eta}{2}\right)\cosh\left(\frac{\eta}{2}\right)}{8\eta[\cosh(\eta) - \cos(\eta)]}. \end{aligned} \tag{20}$$

A comparison of the center temperatures T_c obtained by our DNS and the full and the simplified Hart and Ohlsen [17] model is given in Figs. 8(a) and 8(c). Both Hart and Ohlsen [17] models require the mean-temperature gradient b as input parameter, which can be defined in a variety of ways. We have tested the exact pointwise gradient at the cell center $b = \langle \partial_z T(r = 0)\rangle_t|_{z=H/2}$, at

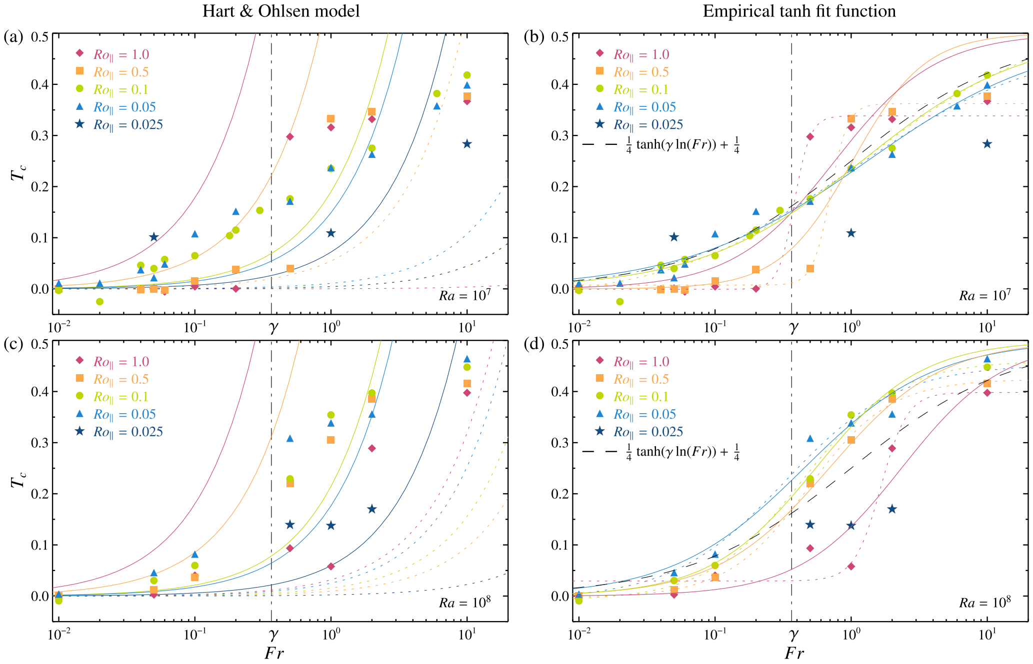

FIG. 8. (a), (c) Comparison of the Hart and Ohlsen [17] model and the center temperature T_c obtained by our DNS as function of Fr. The filled symbols mark $T_c^a \equiv \langle T(r=0, z=H/2)\rangle_t$ from our DNS; the solid lines mark the full Hart and Ohlsen [17] model, and the dotted lines the simplified version given by Eq. (20); (a) $\mathrm{Ra} = 10^7$, (c) $\mathrm{Ra} = 10^8$. (b), (d) The filled symbols are identical to (a); the solid lines correspond to the best fit with four free parameters, Eq. (21); the dotted lines correspond to the best fit with two free parameters, Eq. (22). The black dashed line correspond to the empirical function (23); (b) $\mathrm{Ra} = 10^7$, (d) $\mathrm{Ra} = 10^8$.

the sidewall $b = \langle \partial_z T(r=R,\phi)\rangle_{t,\phi}|_{z=H/2}$, as plane average $b = \langle \partial_z T\rangle_{t,\phi}|_{z=H/2}$, as well as linear fits across different vertical lengths. While these b values can differ in absolute value, their impact on the ultimate result is minor. The best agreement between the models and our DNS was achieved using the plane average, which is used in Figs. 8(a) and 8(c). Our results show that the Hart and Ohlsen [17] model does not capture the correct behavior of T_c for larger values of Fr. Further, T_c in their model can reach unphysical values that exceed T_{top}, as pointed out by Hart and Ohlsen [17].

Here we propose the following empirical fit function to describe the observed T_c^a trends of our DNS data sets in Fig. 8,

$$T_c^{\mathrm{fit}}(\mathrm{Fr}) = A_1 \;\tanh[A_2 \ln(\mathrm{Fr}) + A_3] + A_4. \tag{21}$$

Taking into account that $\lim_{\mathrm{Fr}\to 0} T_c = 0$ and $\lim_{\mathrm{Fr}\to\infty} T_c = T_{\mathrm{bot}} = \frac{1}{2}$, the coefficients A_1 and A_4 can be fixed to $\frac{1}{4}$ and Eq. (21) simplifies further to

$$T_c^{\mathrm{fit}}(\mathrm{Fr}) = \tfrac{1}{4}\tanh(B_1 \ln(\mathrm{Fr}) + B_2) + \tfrac{1}{4}. \tag{22}$$

The resulting best fits are shown in Figs. 8(b) and 8(d) and the fit coefficients are given in Table I. In particular, for the cases in the CC regime, $\mathrm{Ro}_\| \in \{0.1, 0.05\}$, Eqs. (21) and (22) describe $T_c(\mathrm{Fr})$ phenomenologically better than the Hart and Ohlsen [17] model. Based on the obtained coefficients A_i and B_i, we also propose the following expression without fit coefficients:

$$T_c(\mathrm{Fr}) = \tfrac{1}{4}\tanh[\gamma \ln(\mathrm{Fr})] + \tfrac{1}{4}. \tag{23}$$

TABLE I. Fit coefficients for Eqs. (21) and (22), shown in Figs 8(b) and 8(d).

Ra	$\mathrm{Ro}_\parallel$	A_1	A_2	A_3	A_4	B_1	B_2
10^7	0.05	0.245	0.322	−0.021	0.237	0.322	−0.088
	0.1	0.278	0.314	−0.070	0.254	0.365	−0.065
	0.5	0.177	3.373	1.191	0.185	0.815	−0.018
	1.0	0.170	3.688	3.547	0.169	0.584	0.161
10^8	0.05	0.230	0.527	0.594	0.223	0.452	0.360
	0.1	0.235	0.621	0.514	0.226	0.561	0.337
	0.5	0.213	0.726	0.530	0.211	0.528	0.196
	1.0	0.184	2.230	−1.123	0.214	0.578	−0.492

We have not included the data points for $\mathrm{Ro}_\parallel = 0.025$ in these fits since these cases are very close to the onset of convection and, thus, other physical mechanisms such as wall modes dominate [e.g., Refs. [69,82–84]].

III. LOCAL HEAT FLUX MEASUREMENTS

The local heat flux distribution $q = q(r, \phi, z)$ is closely related to the temperature distribution. It is given by

$$q = (\mathrm{Ra}\,\mathrm{Pr}\,\gamma)^{1/2}\langle u_z T\rangle_t - \gamma^{-1}\partial_z\langle T\rangle_t, \tag{24}$$

when expressed within the nondimensionalisation of our DNS [78]. At the top and bottom boundaries the first term is identically zero, and q is solely determined by the temperature gradient. The global heat flux defines the Nusselt number $\mathrm{Nu} \equiv \langle q\rangle_{r,\phi,z}$. For any arbitrary vertical position z_0 also holds $\mathrm{Nu} = \langle q(z = z_0)\rangle_{r,\phi}$ since the horizontally averaged heat flux is constant throughout the domain for long time averages.

Here, we are especially interested in the question of how accurately local temperature measurements can be used to deduce the global Nusselt number in C^3. For this purpose, we compare the local heat flux at both boundaries q_{top} and q_{bot} with the arithmetic mean $(q_{\mathrm{top}} + q_{\mathrm{bot}})/2$ and the full Nu in Fig. 9. Additionally, we also indicate with blue shadings where q_{top} and with pink shadings where q_{bot} deviates by more than ±20% from Nu. The white areas mark the ideal radial positions where a local measurement is close to the actual mean value. In contrast, both colors add up to create a purple shading when both local heat fluxes deviate by more than ±20% from Nu.

In the 3D and QG regimes, i.e., $\mathrm{Fr} < \gamma$, displayed on the left side of Fig. 9, the q_{top} and q_{bot} values are generally good proxies for Nu. Furthermore, the arithmetic average almost perfectly compensates the deviations in the upper and lower local heat flux measurements.

In the centrifugally dominated QC and CC regimes, i.e., $\mathrm{Fr} > \gamma$, local heat flux measurements are unrepresentative of the global values, as was the case for the temperature profiles. With Coriolis force absent, i.e., $\mathrm{Ro}_\parallel = \infty$, the absolute difference is largest due to the imprint that the detachment of the strong central jet of the meridional circulation leaves on the bottom plate and more significantly on the top plate due to the jet's impingement. We find that $q_{\mathrm{top}} > \mathrm{Nu}$ and $q_{\mathrm{bot}} < \mathrm{Nu}$ in the bulk of the cell, $r/R \lesssim 0.6$. The downwelling along the sidewall causes the opposite effect for $r/R \gtrsim 0.6$ but with lower magnitude, such that $q_{\mathrm{top}} < \mathrm{Nu}$ and $q_{\mathrm{bot}} > \mathrm{Nu}$.

With increasing Coriolis force, i.e., decreasing $\mathrm{Ro}_\parallel$, the absolute deviation of q from the value of Nu becomes smaller but the general tendencies remain: in the interior q_{top} overestimates and q_{bot} underestimates Nu, whereas the situation is reversed close to the lateral boundary. The cross-over always occurs in the range $0.5 \lesssim r/R \lesssim 0.8$. For the tornado-like flows in the QC regime, i.e., $\mathrm{Ro}_\parallel = 1$ and 0.1, the helical upflow widens and breaks up before reaching the top boundary layer, hence, there is no strong signature in q_{top}. Further, the central vortex core does not stay fixed but circulates around $r = 0$, which lessens the suppression of q_{bot} compared to the zero Coriolis force cases. In the

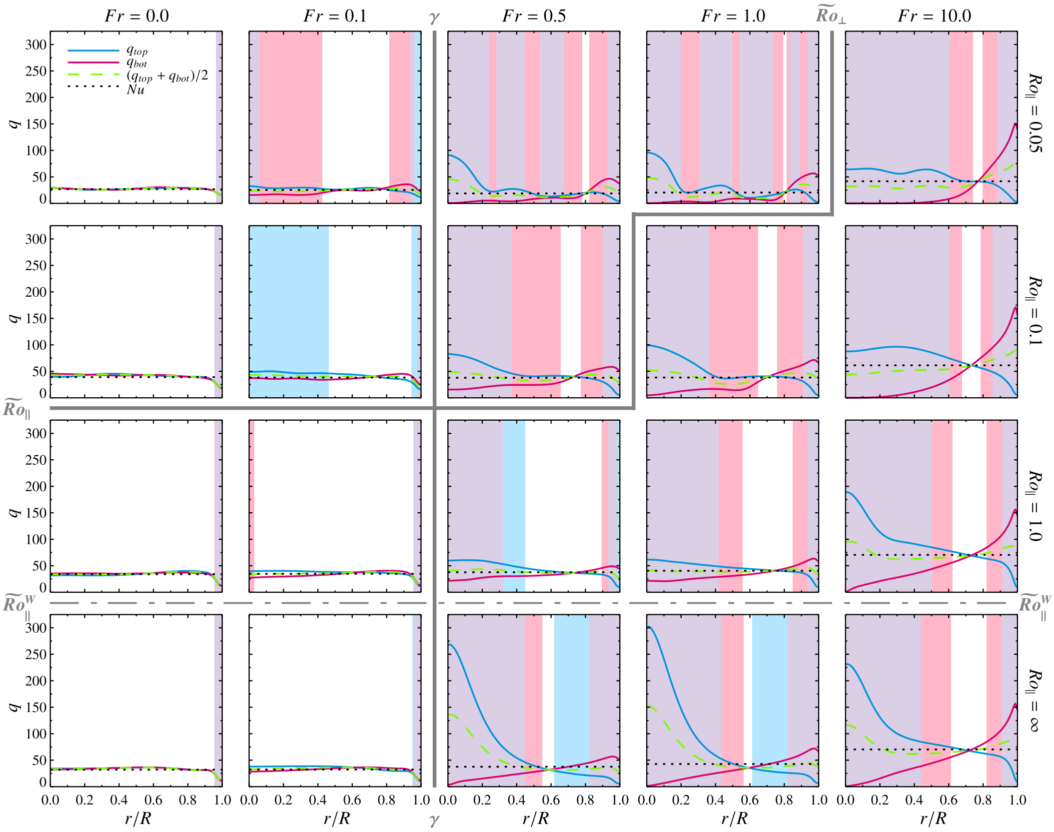

FIG. 9. Local heat fluxes $q_{\rm top}$ (blue line) and $q_{\rm bot}$ (pink line), based on the temperature gradient at the top and bottom plate, respectively. The green long-dashed indicates the average $(q_{\rm top} + q_{\rm bot})/2$. The dotted black line shows the Nusselt number Nu for comparison. The blue shaded area indicates where $|q_{\rm top} - {\rm Nu}|/{\rm Nu} > 0.2$ and the pink area where $|q_{\rm bot} - {\rm Nu}|/{\rm Nu} > 0.2$. Note that purple shading means both local heat fluxes deviate from Nu with more than ±20%.

hurricane-like flows in the QC regime, particularly $\text{Ro}_\parallel = 0.1$, $\text{Fr} = 0.5$ and $\text{Ro}_\parallel = 0.1$, $\text{Fr} = 1.0$, the local heat fluxes also exhibit signs of the ring structure.

In all $\text{Fr} > \gamma$ cases, the arithmetic average of $q_{\rm top}$ and $q_{\rm bot}$ also partially compensates for the local differences. This compensation is best in the range $0.2 \lesssim r/R \lesssim 0.8$. Furthermore, for $\text{Ro}_\parallel < \widetilde{\text{Ro}}_\parallel^W$, and $\text{Fr} > \gamma$, shown in the upper right corner of Fig. 9, the radial range where $q_{\rm top}$ is close to Nu is much larger than $q_{\rm bot}$, as indicated by the separately occurring pink but not blue areas. Thus, the local heat flux in the upper half of the cylinder is generally less affected by centrifugal buoyancy than the local heat flux in the lower half. This is in line with the findings related to the vertical temperature profiles in Fig. 6.

In our DNS, the top and bottom boundaries are infinitesimally thin and perfectly isothermal. In the laboratory, this is only approximately true. Instead, a heat flux is often imposed and Ra and Nu are inferred by measuring Δ using a finite number of pointwise measurements in the top and bottom plates to approximate $T_{\rm bot}$ and $T_{\rm top}$. However, Calkins *et al.* [85] have shown that thermal boundary conditions are asymptotically equivalent in the rapidly rotating case. The mechanical boundary conditions are more important [6,64]; they are no-slip in most experiments and in our DNS. Thus, we argue that our DNS results for the local heat flux translate to laboratory experiments. The optimal radial positions for thermal measurements to experimentally determine Ra and Nu are at $0.2 \lesssim r/R \lesssim 0.8$.

IV. CONCLUDING REMARKS

Our rotating convection DNS with the full inertial term have shown that centrifugal buoyancy affects the flow due to the complex interplay of the LSC, plumes, convective Taylor columns and the meridional circulation. This complexity is reflected in strongly radially and vertically dependent temperature distributions, as well as in the local heat fluxes distributions. We have verified that the regimes of the C^3 system (3D, QG, QC, and CC) can be identified in the sidewall and center temperatures, extending the Nusselt number based characterization of Horn and Aurnou [16]. Further, our DNS results have been employed to test the seminal model of Hart and Ohlsen [17] for the center temperature in a wide Fr and $\mathrm{Ro}_\parallel$ space. We have shown that their model does not capture the correct behavior of T_c for larger Fr. Our proposed empirical tanh fit functions better reproduce the dependencies of T_c on Fr. The discrepancy between the Hart and Ohlsen [17] model and the empirical fit demonstrates that there is a pressing need for new theory.

Our DNS results can be utilized as a guide for rapidly rotating convection laboratory experiments. Most importantly, our results show that centrifugal buoyancy effects do not significantly alter the temperature profiles or the heat flux measurements in experiments with $\mathrm{Fr} \lesssim \gamma$. In contrast, for $\mathrm{Fr} \gtrsim \gamma$, we have found that the local profiles $\bar{T}_l(r,z)$ are strongly dependent on the radial position. However, for $\mathrm{Fr} > \gamma$ and $\mathrm{Ro}_\parallel \gtrsim \widetilde{\mathrm{Ro}}_\parallel$, the local profiles for $r/R \gtrsim 0.2$ in the upper part of the domain are less altered by centrifugal buoyancy than the profiles in the lower part; the strongest centrifugal buoyancy effects can be detected close to the the axis $r/R \lesssim 0.2$. For $\mathrm{Fr} > \gamma$ and $\mathrm{Ro}_\parallel \lesssim \widetilde{\mathrm{Ro}}_\parallel$, it is not possible to identify a single radial position for which $\bar{T}_l(r,z)$ approximates $\bar{T}(z)$.

To estimate optimal radial positions for measuring heat fluxes in laboratory settings, we have evaluated the radial dependencies of the local heat fluxes at the top and bottom boundaries of our DNS solutions (Fig. 9). In high Fr cases, local heat flux measurements greatly differ between the top and bottom boundaries. Much to our pleasant surprise, the strong radial dependencies of q_{top} and q_{bot} can cancel out in the arithmetic mean $(q_{\mathrm{top}} + q_{\mathrm{bot}})/2$ (Fig. 9, green dashed line). As a consequence, local temperature measurements in the range $0.2 \lesssim r/R \lesssim 0.8$ can provide reliable proxies for Δ and, hence, for Ra and Nu. High Fr measurements at the central point $r = 0$ and at the sidewall $r = R$ must, however, be treated with caution.

ACKNOWLEDGMENTS

S.H. and J.M.A. thank the NSF Geophysics Program, Awards No. 1547269 and No. 1853196. S.H. acknowledges funding by the Deutsche Forschungsgemeinschaft (DFG, German Research Foundation) Project No. HO 5890/1-1 and the Leibniz-Rechenzentrum for providing computational resources on SuperMUC.

[1] J. M. Aurnou, M. A. Calkins, J. S. Cheng, K. Julien, E. M. King, D. Nieves, K. M. Soderlund, and S. Stellmach, Rotating convective turbulence in Earth and planetary cores, Phys. Earth Planet. Inter. **246**, 52 (2015).

[2] K. Julien, E. Knobloch, A. M. Rubio, and G. M. Vasil, Heat Transport in Low-Rossby-Number Rayleigh-Bénard Convection, Phys. Rev. Lett. **109**, 254503 (2012).

[3] K. Julien, A. M. Rubio, I. Grooms, and E. Knobloch, Statistical and physical balances in low Rossby number Rayleigh–bénard convection, Geophys. Astrophys. Fluid Dyn. **106**, 392 (2012).

[4] J. S. Cheng, J. M. Aurnou, K. Julien, and R. P. J. Kunnen, A heuristic framework for next-generation models of geostrophic convective turbulence, Geophys. Astrophys. Fluid Dyn. **112**, 277 (2018).

[5] J. S. Cheng, S. Stellmach, A. Ribeiro, A. Grannan, E. M. King, and J. M. Aurnou, Laboratory-numerical models of rapidly rotating convection in planetary cores, Geophys. J. Int. **201**, 1 (2015).

[6] S. Stellmach, M. Lischper, K. Julien, G. Vasil, J. S. Cheng, A. Ribeiro, E. M. King, and J. M. Aurnou, Approaching the Asymptotic Regime of Rapidly Rotating Convection: Boundary Layers Versus Interior Dynamics, Phys. Rev. Lett. **113**, 254501 (2014).

[7] R. P. J. Kunnen, R. Ostilla-Mónico, E. P. van der Poel, R. Verzicco, and D. Lohse, Transition to geostrophic convection: The role of the boundary conditions, J. Fluid Mech. **799**, 413 (2016).

[8] R. E. Ecke and J. J. Niemela, Heat Transport in the Geostrophic Regime of Rotating Rayleigh-Bénard Convection, Phys. Rev. Lett. **113**, 114301 (2014).

[9] S. Chandrasekhar and D. D. Elbert, The instability of a layer of fluid heated below and subject to Coriolis forces. II, Proc. R. Soc. A **231**, 198 (1955).

[10] G. Ahlers, E. Brown, F. Fontenele Araujo, D. Funfschilling, S. Grossmann, and D. Lohse, Non-Oberbeck–Boussinesq effects in strongly turbulent Rayleigh–Bénard convection, J. Fluid Mech. **569**, 409 (2006).

[11] S. Horn and O. Shishkina, Rotating non-Oberbeck–Boussinesq Rayleigh–Bénard convection in water, Phys. Fluids **26**, 055111 (2014).

[12] S. Horn, O. Shishkina, and C. Wagner, On non-Oberbeck–Boussinesq effects in three-dimensional Rayleigh–Bénard convection in glycerol, J. Fluid Mech. **724**, 175 (2013).

[13] K. Sugiyama, E. Calzavarini, S. Grossmann, and D. Lohse, Flow organization in two-dimensional non-Oberbeck–Boussinesq Rayleigh-Bénard convection in water, J. Fluid Mech. **637**, 105 (2009).

[14] K. Sugiyama, E. Calzavarini, S. Grossmann, and D. Lohse, Non-Oberbeck–Boussinesq effects in two-dimensional Rayleigh-Bénard convection in glycerol, Europhys. Lett. **80**, 34002 (2007).

[15] S. Weiss, X. He, G. Ahlers, E. Bodenschatz, and O. Shishkina, Bulk temperature and heat transport in turbulent Rayleigh–Bénard convection of fluids with temperature-dependent properties, J. Fluid Mech. **851**, 374 (2018).

[16] S. Horn and J. M. Aurnou, Regimes of Coriolis-Centrifugal Convection, Phys. Rev. Lett. **120**, 204502 (2018).

[17] J. E. Hart and D. R. Ohlsen, On the thermal offset in turbulent rotating convection, Phys. Fluids **11**, 2101 (1999).

[18] J. E. Hart, On the influence of centrifugal buoyancy on rotating convection, J. Fluid Mech. **403**, 133 (2000).

[19] M. A. Torrest and J. L. Hudson, The effect of centrifugal convection on the stability of a rotating fluid heated from below, Appl. Sci. Res. **29**, 273 (1974).

[20] G. M. Homsy and J. L. Hudson, Centrifugal convection and its effect on the asymptotic stability of a bounded rotating fluid heated from below, J. Fluid Mech. **48**, 605 (1971).

[21] J. M. Lopez, A. Rubio, and F. Marques, Travelling circular waves in axisymmetric rotating convection, J. Fluid Mech. **569**, 331 (2006).

[22] J. M. Lopez and F. Marques, Centrifugal effects in rotating convection: Nonlinear dynamics, J. Fluid Mech. **628**, 269 (2009).

[23] J. Curbelo, J. M. Lopez, A. M. Mancho, and F. Marques, Confined rotating convection with large Prandtl number: Centrifugal effects on wall modes, Phys. Rev. E **89**, 013019 (2014).

[24] F. Marques, I. Mercader, O. Batiste, and J. M. Lopez, Centrifugal effects in rotating convection: Axisymmetric states and three-dimensional instabilities, J. Fluid Mech. **580**, 303 (2007).

[25] N. Becker, J. D. Scheel, M. C. Cross, and G. Ahlers, Effect of the centrifugal force on domain chaos in Rayleigh-Bénard convection, Phys. Rev. E **73**, 066309 (2006).

[26] E. M. King, S. Stellmach, J. Noir, U. Hansen, and J. M. Aurnou, Boundary layer control of rotating convection systems, Nature **457**, 301 (2009).

[27] R. P. J. Kunnen, H. J. H. Clercx, and G. J. F. van Heijst, The structure of sidewall boundary layers in confined rotating Rayleigh–Bénard convection, J. Fluid Mech. **727**, 509 (2013).

[28] O. Shishkina, R. J. A. M. Stevens, S. Grossmann, and D. Lohse, Boundary layer structure in turbulent thermal convection and its consequences for the required numerical resolution, New J. Phys. **12**, 075022 (2010).

[29] D. D. Gray and A. Giorgini, The validity of the Boussinesq approximation for liquids and gases, Int. J. Heat Mass Transf. **19**, 545 (1976).

[30] O. Shishkina, S. Horn, S. Wagner, and E. S. C. Ching, Thermal Boundary Layer Equation for Turbulent Rayleigh–Bénard Convection, Phys. Rev. Lett. **114**, 114302 (2015).

[31] S. Weiss, R. J. A. M. Stevens, J.-Q. Zhong, H. J. H. Clercx, D. Lohse, and G. Ahlers, Finite-Size Effects Lead to Supercritical Bifurcations in Turbulent Rotating Rayleigh–Bénard Convection, Phys. Rev. Lett. **105**, 224501 (2010).

[32] S. Weiss and G. Ahlers, Heat transport by turbulent rotating Rayleigh–Bénard convection and its dependence on the aspect ratio, J. Fluid Mech. **684**, 205 (2011).

[33] G. Ahlers, S. Grossmann, and D. Lohse, Heat transfer and large scale dynamics in turbulent Rayleigh-Bénard convection, Rev. Mod. Phys. **81**, 503 (2009).

[34] I. Grooms, K. Julien, J. B. Weiss, and E. Knobloch, Model of Convective Taylor Columns in Rotating Rayleigh-Bénard Convection, Phys. Rev. Lett. **104**, 224501 (2010).

[35] E. M. King and J. M. Aurnou, Thermal evidence for Taylor columns in turbulent rotating Rayleigh-Bénard convection, Phys. Rev. E **85**, 016313 (2012).

[36] R. J. A. M. Stevens, H. J. H. Clercx, and D. Lohse, Heat transport and flow structure in rotating Rayleigh–Bénard convection, Eur. J. Mech. (B/Fluids) **40**, 41 (2013).

[37] E. M. King, S. Stellmach, and J. M. Aurnou, Heat transfer by rapidly rotating Rayleigh–Bénard convection, J. Fluid Mech. **691**, 568 (2012).

[38] R. P. J. Kunnen, R. J. A. M. Stevens, J. Overkamp, C. Sun, G. F. van Heijst, and H. J. H. Clercx, The role of Stewartson and Ekman layers in turbulent rotating Rayleigh–Bénard convection, J. Fluid Mech. **688**, 422 (2011).

[39] K. Julien, S. Legg, J. McWilliams, and J. Werne, Rapidly rotating turbulent Rayleigh–Bénard convection, J. Fluid Mech. **322**, 243 (1996).

[40] F. Chillá, S. Ciliberto, and C. Innocenti, Thermal boundary layer in turbulent thermal convection, Europhys. Lett. **22**, 681 (1993).

[41] Y. Liu and R. E. Ecke, Heat transport measurements in turbulent rotating Rayleigh-Bénard convection, Phys. Rev. E **80**, 036314 (2009).

[42] Y. Liu and R. E. Ecke, Local temperature measurements in turbulent rotating Rayleigh-Bénard convection, Phys. Rev. E **84**, 016311 (2011).

[43] G. Ahlers, E. Bodenschatz, D. Funfschilling, S. Grossmann, X. He, D. Lohse, R. J. A. M. Stevens, and R. Verzicco, Logarithmic Temperature Profiles in Turbulent Rayleigh-Bénard Convection, Phys. Rev. Lett. **109**, 114501 (2012).

[44] X. He, D. P. M. van Gils, E. Bodenschatz, and G. Ahlers, Logarithmic Spatial Variations and Universal f^{-1} Power Spectra of Temperature Fluctuations in Turbulent Rayleigh-Bénard Convection, Phys. Rev. Lett. **112**, 174501 (2014).

[45] A. Tilgner, A. Belmonte, and A. Libchaber, Temperature and velocity profiles of turbulent convection in water, Phys. Rev. E **47**, R2253 (1993).

[46] O. Shishkina and A. Thess, Mean temperature profiles in turbulent Rayleigh–Bénard convection of water, J. Fluid Mech. **633**, 449 (2009).

[47] Q. Zhou, R. J. A. M. Stevens, K. Sugiyama, S. Grossmann, D. Lohse, and K.-Q. Xia, Prandtl–Blasius temperature and velocity boundary-layer profiles in turbulent Rayleigh-Bénard convection, J. Fluid Mech. **664**, 297 (2010).

[48] E. Brown and G. Ahlers, Temperature gradients, and search for non-Boussinesq effects, in the interior of turbulent Rayleigh–Bénard convection, Europhys. Lett. **80**, 14001 (2007).

[49] S.-L. Lui and K.-Q. Xia, Spatial structure of the thermal boundary layer in turbulent convection, Phys. Rev. E **57**, 5494 (1998).

[50] R. Du Puits, C. Resagk, A. Tilgner, F. H. Busse, and A. Thess, Structure of thermal boundary layers in turbulent Rayleigh–Bénard convection, J. Fluid Mech. **572**, 231 (2007).

[51] M. S. Emran and J. Schumacher, Fine-scale statistics of temperature and its derivatives in convective turbulence, J. Fluid Mech. **611**, 13 (2008).

[52] J. D. Scheel and J. Schumacher, Local boundary layer scales in turbulent Rayleigh–Bénard convection, J. Fluid Mech. **758**, 344 (2014).

[53] J. Schumacher, V. Bandaru, A. Pandey, and J. D. Scheel, Transitional boundary layers in low-Prandtl-number convection, Phys. Rev. Fluids **1**, 084402 (2016).

[54] D. Nieves, A. M. Rubio, and K. Julien, Statistical classification of flow morphology in rapidly rotating Rayleigh-Bénard convection, Phys. Fluids **26**, 086602 (2014).

[55] G. Ahlers, X. He, D. Funfschilling, and E. Bodenschatz, Heat transport by turbulent Rayleigh–Bénard convection for $\mathrm{Pr} \simeq 0.8$ and $3 \times 10^{12} \lesssim \mathrm{Ra} \lesssim 10^{15}$: Aspect ratio $\Gamma = 0.50$, New J. Phys. **14**, 103012 (2012).

[56] S. Grossmann and D. Lohse, Logarithmic temperature profiles in the ultimate regime of thermal convection, Phys. Fluids **24**, 125103 (2012).

[57] X. He, D. Funfschilling, H. Nobach, E. Bodenschatz, and G. Ahlers, Transition to the Ultimate State of Turbulent Rayleigh-Bénard Convection, Phys. Rev. Lett. **108**, 024502 (2012).

[58] A. Belmonte, A. Tilgner, and A. Libchaber, Temperature and velocity boundary layers in turbulent convection, Phys. Rev. E **50**, 269 (1994).

[59] K.-Q. Xia, S. Lam, and S.-Q. Zhou, Heat-Flux Measurement in High-Prandtl-Number Turbulent Rayleigh-Bénard Convection, Phys. Rev. Lett. **88**, 064501 (2002).

[60] T. Vogt, S. Horn, A. M. Grannan, and J. M. Aurnou, Jump rope vortex in liquid metal convection, Proc. Natl. Acad. Sci. USA **115**, 12674 (2018).

[61] R. J. A. M. Stevens, H. J. H. Clercx, and D. Lohse, Breakdown of the large-scale circulation in $\Gamma = 1/2$ rotating Rayleigh-Bénard flow, Phys. Rev. E **86**, 056311 (2012).

[62] S. Horn and O. Shishkina, Toroidal and poloidal energy in rotating Rayleigh–Bénard convection, J. Fluid Mech. **762**, 232 (2015).

[63] R. P. J. Kunnen, H. J. H. Clercx, and B. J. Geurts, Breakdown of large-scale circulation in turbulent rotating convection, Europhys. Lett. **84**, 24001 (2008).

[64] R. P. J. Kunnen, H. J. H. Clercx, and B. J. Geurts, Heat flux intensification by vortical flow localization in rotating convection, Phys. Rev. E **74**, 056306 (2006).

[65] R. P. J. Kunnen, B. J. Geurts, and H. J. H. Clercx, Experimental and numerical investigation of turbulent convection in a rotating cylinder, J. Fluid Mech. **642**, 445 (2010).

[66] R. J. A. M. Stevens, H. J. H. Clercx, and D. Lohse, Optimal Prandtl number for heat transfer in rotating Rayleigh-Bénard convection, New J. Phys. **12**, 075005 (2010).

[67] J.-Q. Zhong and G. Ahlers, Heat transport and the large-scale circulation in rotating turbulent Rayleigh-Bénard convection, J. Fluid Mech. **665**, 300 (2010).

[68] J.-Q. Zhong, R. J. A. M. Stevens, H. J. H. Clercx, R. Verzicco, D. Lohse, and G. Ahlers, Prandtl-, Rayleigh-, and Rossby-Number Dependence of Heat Transport in Turbulent Rotating Rayleigh-Bénard Convection, Phys. Rev. Lett. **102**, 044502 (2009).

[69] S. Horn and P. J. Schmid, Prograde, retrograde, and oscillatory modes in rotating Rayleigh-Bénard convection, J. Fluid Mech. **831**, 182 (2017).

[70] J.-Q. Zhong, H.-M. Li, and X.-Y. Wang, Enhanced azimuthal rotation of the large-scale flow through stochastic cessations in turbulent rotating convection with large Rossby numbers, Phys. Rev. Fluids **2**, 044602 (2017).

[71] O. Shishkina and S. Horn, Thermal convection in inclined cylindrical containers, J. Fluid Mech. **790**, R3 (2016).

[72] O. Shishkina, Momentum and heat transport scalings in laminar vertical convection, Phys. Rev. E **93**, 051102(R) (2016).

[73] D. S. Nolan and B. F. Farrell, The structure and dynamics of tornado-like vortices, J. Atmos. Sci. **56**, 2908 (1999).

[74] N. B. Ward, The exploration of certain features of tornado dynamics using a laboratory model, J. Atmos. Sci. **29**, 1194 (1972).

[75] B. Fiedler, Suction vortices and spiral breakdown in numerical simulations of tornado-like vortices, Atmos. Sci. Lett. **10**, 109 (2009).

[76] H. B. Bluestein, *Severe Convective Storms and Tornadoes* (Springer, Berlin, 2013).

[77] S. Nong and K. Emanuel, A numerical study of the genesis of concentric eyewalls in hurricanes, Q. J. R. Meteorol. Soc. **129**, 3323 (2003).

[78] O. Shishkina and C. Wagner, Local heat fluxes in turbulent Rayleigh-Bénard convection, Phys. Fluids **19**, 085107 (2007).

[79] I. B. Duncan, Axisymmetric convection between two rotating disks, J. Fluid Mech. **24**, 417 (1966).

[80] J. L. Hudson, Non-isothermal flow between rotating disks, Chem. Eng. Sci. **23**, 1007 (1968).

[81] See Supplemental Material at http://link.aps.org/supplemental/10.1103/PhysRevFluids.4.073501 for the full solution of the Hart and Ohlsen model and a `fortran` routine that numerically solves for the center temperature.

[82] F. Zhong, R. Ecke, and V. Steinberg, Asymmetric Modes and the Transition to Vortex Structures in Rotating Rayleigh-Bénard Convection, Phys. Rev. Lett. **67**, 2473 (1991).

[83] R. E. Ecke, F. Zhong, and E. Knobloch, Hopf bifurcation with broken reflection symmetry in rotating Rayleigh-Bénard convection, Europhys. Lett. **19**, 177 (1992).

[84] H. F. Goldstein, E. Knobloch, I. Mercader, and M. Net, Convection in a rotating cylinder. Part 1 Linear theory for moderate Prandtl numbers, J. Fluid Mech. **248**, 583 (1993).

[85] M. A. Calkins, K. Hale, K. Julien, D. Nieves, D. Driggs, and P. Marti, The asymptotic equivalence of fixed heat flux and fixed temperature thermal boundary conditions for rapidly rotating convection, J. Fluid Mech. **784**, R2 (2015).